Draft version April 2, 2025
Typeset using LaTeX **twocolumn** style in AASTeX631

Investigating HII Regions in the Disk of NGC 7331 with the Circumgalactic Hα Spectrograph

Nazende ipek Kerkeser,[1] Nicole Melso,[1] David Schiminovich,[2,3] Erika Hamden,[1] Meghna Sitaram,[2,3] and Ignacio Cevallos-Aleman[3,4]

[1]Steward Observatory, University of Arizona, 933 N. Cherry Avenue, Tucson, AZ 85721, USA
[2]Department of Astronomy, Columbia University, 550 W. 120th Street MC 5246, New York, NY 10027, USA
[3]Columbia Astrophysics Laboratory, Columbia University, 550 W. 120th St. MC 5247, New York, NY 10027, USA
[4]Department of Physics, Columbia University, 538 W. 120th Street 704 Pupin Hall MC 5255, New York, NY 10027, USA

ABSTRACT

We investigate the ionized gas kinematics of HII regions in the disk of NGC 7331 using IFU data collected with the Circumgalactic Hα Spectrograph (CHαS). NGC 7331 is a well-studied nearby galaxy with HII regions resolved by seeing-limited observations, making it ideally suited for this work. The galaxy disk features vigorous star formation (2.987 $M_\odot$ yr^{-1}), especially in the central ring of starburst activity. Our catalog of > 150 HII regions is drawn from a large database of HII regions identified in past literature, selecting regions well matched to our spatial resolution. Using this refined catalog, we perform aperture photometry on the SIRTF Nearby Galaxies Survey (SINGS) narrowband Hα images of NGC 7331, extracting the Hα luminosity L(Hα) of 155 HII regions. We present corresponding measurements of the average line-of-sight ionized gas velocity dispersion σ in these regions with CHαS. High-resolution velocity and dispersion maps of the galactic disk are produced from the CHαS spectral imaging, selecting spaxels with high signal-to-noise in order to measure velocity dispersions as low as 12 km s^{-1}. Our measurements of the L(Hα), $\Sigma_{\rm SFR}$ and σ in NGC 7331 are consistent with spatially resolved observations of HII regions in large surveys of nearby galaxies. We explore the L(Hα) $-\sigma$ relationship, identifying turbulent HII regions with non-thermal dispersions likely driven by stellar feedback. The dispersion is correlated with the star formation rate surface density, and using the relation $\sigma \propto \epsilon \Sigma_{\rm SFR}^{\alpha}$, HII regions in NGC7331 are best fit by $\epsilon = 80$, $\alpha = 0.335$.

Keywords: HII regions, Interstellar line emission, Spectroscopy, Spiral galaxies

1. INTRODUCTION

HII regions are ionized pockets of gas within galaxies, formed when intense radiation from young, massive stars strips electrons from surrounding hydrogen atoms. These regions serve as vital tracers of recent star formation and provide key insights into the interaction between stellar feedback and the interstellar medium (ISM). The ISM across redshifts is supersonically turbulent (Glazebrook 2013; Übler et al. 2019; Bacchini et al. 2020; Rizzo et al. 2024), driven by a combination of interal and external processes including stellar feedback (winds, supernovae), gravitational and magnetic instabilities, galactic shear, and accretion (Elmegreen & Scalo 2004; Glazebrook 2013, & references therein). Turbulence in the interstellar medium plays a crucial role in regulating star formation, providing global pressure support that counteracts gravity while also creating perturbations that provoke small-scale collapse (Mac Low & Klessen 2004). Turbulent motions in the ISM are observationally probed using the gas velocity dispersion, with many studies finding a positive correlation between gas dispersion and star formation rate (Lehnert et al. 2009, 2013; Green et al. 2010, 2014; Le Tiran et al. 2011; Moiseev et al. 2015). This relationship has been studied extensively in high-redshift galaxies and local luminous and ultraluminous infrared galaxies (LIRGs/ULIRGs) with high star formation rates and large gas dispersions (e.g. Bellocchi et al. 2013; Green et al. 2014; Arribas et al. 2014; Übler et al. 2019; Perna et al. 2022) where gravitational instability, gas transport, and external accretion likely contribute significantly to turbulence (Krumholz et al. 2018; Ginzburg et al. 2022; Mai et al. 2024). Galaxies with lower star formation rates around a few $M_\odot$ yr^{-1} may straddle the boundary between gravity-driven turbulence and stellar feedback-driven models where the the ionized gas dispersions are dominated by the internal motions of the HII regions, highlighting the importance of spatially resolved datasets in this regime at low-redshifts (Krumholz & Burkhart 2016). While the connection between gas dispersion and star formation rate is well-established in statistical samples, star formation environments can vary drastically within individual galaxies. Case studies in galaxies with spatially varying star formation environments are crucial to understanding the role turbulence plays in regulating star formation in diverse environments across the galactic disk.

NGC 7331 provides an interesting mixture of environments for investigating the relationship between star formation and ISM gas kinematics, aided by its close proximity (14.5 Mpc, Freedman et al. 2001) and its extensive observation history. Comprehensive observations across wavelengths have identified distinct morphological features in NGC 7331. The galactic disk is bright in Hα emission and hosts a large population of HII regions (Rubin et al. 1965; Hodge & Kennicutt 1983; Marcelin et al. 1994; Petit 1998). A central ring of dust and gas in the disk of NGC 7331 is seen prominently in CO (Young & Scoville 1982), HI (Bosma 1978), IR (Telesco et al. 1982; Regan et al. 2004), and Hα (Battaner et al. 2003). This ring exhibits starburst activity and hosts a significant fraction of the star formation occurring in the galaxy (Battaner et al. 2003; Thilker et al. 2007). Some kinematic studies of NGC 7331 suggest a counter-rotating bulge relative to the disk (Prada et al. 1996), and peculiar velocities at the inner boundary of the central ring are consistent with ionized gas inflow (Battaner et al. 2003). A large-scale warp in the HI gas distribution (Bosma 1978), an extended distribution of debris/plumes/streams surrounding the galaxy, as well as a a large population of dwarf companions, all suggest a history of mergers and tidal interactions (Ludwig et al. 2012; Blauensteiner et al. 2017). Complex velocity structure and morphology combined with active star formation in NGC 7331 provides an ideal setting for studying how star formation influences and is influenced by gas kinematics at moderate spatial resolution. A seeing-limited spatial resolution of $2''$ corresponds to a physical scale of approximately 150 pc in the disk of NGC 7331, allowing detailed resolution of individual HII regions. The HII regions studied in this work have a radius of 173 pc on average.

We present new maps of the complex kinematics in the disk of NGC 7331 using the Circumgalactic Hα Spectrograph (CHαS, Melso et al. 2022). CHαS is an advanced integral field spectrograph optimized for mapping the spatial and kinematic structure of faint, ionized gas. With a resolving power of $R \sim 10,000$, a field of view of $10' \times 10'$, and high sensitivity to very faint emission, CHαS can capture spectral images of nearby galaxy disks at high signal-to-noise with superb survey speed. Integral field spectroscopy (IFS) is a crucial observational technique for establishing large catalogs of resolved HII regions in nearby galaxies and probing the properties of these regions in great detail (e.g., Sánchez et al. 2012; Espinosa-Ponce et al. 2020; McLeod et al. 2020; Cosens et al. 2022; Congiu et al. 2023; Groves et al. 2023; Rickards Vaught et al. 2024). CHαS excels in this regard, efficiently surveying the low-redshift universe by slicing the wide field of view into tens of thousands of spectra collected simultaneously at moderate spectral resolution around a single emission line. CHαS is capable of detecting high-surface-brightness Hα emission from HII regions in the galactic disk in a 6-minute exposure, and it can measure faint emission down to 1 Rayleigh from diffuse gas at the disk-halo interface in just a few hours (Melso et al. 2022). En-route to ultra-deep observations probing the diffuse outskirts of galaxies, CHαS will provide detailed spatial and kinematic characterization of the dense interstellar medium. The maps of NGC 7331 presented in this work are an early demonstration of the full observing power of ChαS.

In this work, we examine the kinematics of HII regions across the disk of NGC 7331, focusing on the relationship between Hα luminosity and ionized gas velocity dispersion (σ). In Section 2, we present the photometric and spectroscopic datasets used in this study, along with the data acquisition and reduction procedures. Section 3 details the methodology for selecting the HII region catalog, including the criteria applied to identify and characterize the regions. In Section 4 we investigate the ionized gas morphology and discuss the analysis of the Hα luminosity and velocity dispersion relationship. In Section 5, we interpret our findings in the context of existing literature and theoretical models, and Section 6 concludes the paper with a summary of key results and directions for future research.

2. OBSERVATIONS

This work relies on a combination of photometric and spectroscopic datasets, detailed below. NGC 7331 has a wealth of multi-wavelength observations, and many of these datasets have aided our analysis. Here we map the spatio-kinematic structure of ionized gas throughout the galactic disk of NGC 7331 in great detail.

2.1. *CHαS Observations*

Spectroscopic data was collected with the recently commissioned Circumgalactic Hα Spectrograph (CHαS). The entrance to the IFS is a microlens array, which segments the telescope focal plane into $> 60,000$

spectra, each dispersed over a narrow bandpass to avoid overlap. CHαS is optimized for mapping the spatial and kinematic structure of ultra-faint ionized gas, so it can easily detect high Hα surface brightness HII regions in the disks of nearby galaxies and resolve complex morphology that can be difficult to fully capture with long-slit spectroscopy. See Melso et al. (2022) for a detailed description of the instrument.

In Figure 1 we present spectral imaging of NGC 7331 in Ha emission. A summary of the CHαS observations is given in Table 1. This data was collected during the Fall of 2023, under very dark, photometric conditions with $< 2\%$ Moon illumination and $> 125°$ Moon separation. The stack shown in Figure 1 consists of 360s exposures co-aligned and co-added to create a two-hour integration. The narrowband filter combination used for these observations has a bandpass of 20 Å FWHM and a central wavelength of 6582 Å. Accordingly, this filter set is best suited for radial velocities ranging from 412 km s^{-1} to 1323 km s^{-1}. The systemic velocity of NGC 7331 ($V_{sys} = 816$ km s^{-1}) is near the center of the filter bandpass, and the galaxy HI line width at 20% of the maximum intensity ($W_{20} = 530$ km s^{-1}) falls within the filter FWHM (Tully 1988; de Vaucouleurs et al. 1991). This filter combination isolates the Hα emission line and rejects contamination from the NII doublet (6573 Å, 6608 Å). The bandpass still includes emission from the sky background, notably the bright OH 6-1P1e,1f (4.5) telluric line (unresolved doublet) at 6578 Å (Osterbrock et al. 1996).

2.2. *Ancillary Data*

This work utilizes multi-wavelength observations of NGC 7331, including the narrowband Hα imaging from the SIRTF Nearby Galaxies Survey (SINGS) (Kennicutt et al. 2003; SINGS Team 2020). HII region flux estimates were derived using the corrected SINGS NGC 7331 Hα map published in Leroy et al. (2012). This map has been corrected for NII contamination and Galactic extinction, and the integrated flux has been matched to values in the literature. The HI 21cm velocity field (moment 1) from The HI Nearby Galaxy Survey (THINGS) (Walter et al. 2008) was used as a reference to create the CHαS velocity map. We also compare with the BIMA Survey of Nearby Galaxies (BIMA SONG) CO (1-0) map (Helfer et al. 2003) in order to identify HII regions located within the gaseous inner ring.

3. METHODS

We detail the methods for extracting kinematic and photometric properties of HII regions from both the CHαS and SINGS data.

3.1. *CHαS Data Reduction*

The stack shown in Figure 1 was created by aligning and averaging multiple exposures, all taken within the same night (See Table 1). The drift between exposures was calculated using the cross-correlation in a high signal-to-noise patch of the disk, and the image registration was performed to sub-pixel precision. The World Coordinate System (WCS) applied to the CHαS data is centered on the wavelength of Hα at the systemic velocity of NGC 7331 adjusted for the heliocentric velocity correction. This solution ensures the best average alignment between the CHαS spectral imaging in Hα emission and narrowband Hα imaging from other surveys. The stacked CHαS data still contains the bright telluric line at 6578 Å. Due to the repeating grid nature of the CHαS spectra, it is important to remove this line, as it fully overlaps Hα emission from ionized gas at 685 km s^{-1} and 1180 km s^{-1} and partially overlaps emission at multiple intermediate velocities within the bandpass. We collect separate sky data at a pointing offset from NGC 7331 and use that sky stack to create the background subtracted image shown in Figure 1. Since the absolute flux measurements are done using the SINGS Hα data (see Section 3.4) we do not apply a flux calibration to the CHαS data in this work. We do correct by an average flat field in order to ensure that relative measurements across the CHαS stack are consistent. Throughout this work in order to convert from pixels to km s^{-1} we use the CHαS linear dispersion mapping. The CHαS linear dispersion varies along the spectral direction; however, the major axis of NGC 7331 is aligned with the cross-spectral direction and variation in the linear dispersion across the disk is a very small effect on the order of < 1 km s^{-1} error. We extract and average the linear dispersion values at lenslet positions that cover the disk of NGC 7331, resulting in an average linear dispersion of 0.37 Å pix^{-1} or 16.86 km s^{-1} pix^{-1} used in this work. The CHαS data reduction pipeline is a work in progress (see updates in Cevallos-Aleman et al. 2024).

3.2. *CHαS Spectral Extraction and Fitting*

The CHαS field of view consists of $> 60,000$ spectra, one for each lenslet in the microlens array. NGC 7331 covers approximately 3000 lenslets, and ~ 1400 of the spectra extracted from these lensets meet our SNR requirements. We extract these spectra using rectangular apertures centered on the detected Hα emission, collapsing each spectrum along the cross-spectral direction to improve the S/N. The mean (velocity centroid) and standard deviation (dispersion) are calculated from the 1D Gaussian fit to the Hα emission line in each spectrum. All lines were fit as a single component (one mean velocity peak with a single dispersion value). We calculate the Doppler shift of the Hα emission line and the corresponding ionized gas velocity by measuring the offset between the Hα emission line peak and the peak emission from the stationary telluric line in the sky background image. The standard deviation of the 1D Gaussian fit to each Hα emission line is the the observed dispersion (σ_{obs}). We subtract the instrument line profile (σ_{inst}) from the observed dispersion (σ_{obs}) in quadrature. We similarly correct for thermal broadening at a gas temperature of 10^4 K ($\sigma_b = 9.1$ km s^{-1}) (Rozas et al. 2000). The line-of-sight ionized gas dispersion calculation used in this work follows Equation 1.

$$\sigma = \sqrt{(\sigma_{obs})^2 - (\sigma_{inst})^2 - (\sigma_b)^2} \quad (1)$$

We note that in theory we should also correct for the natural line width of Hα emission ($\sigma_N = 3$ km s^{-1}); however, the instrument line profile is measured by stacking the sky spectra extracted from each lenslet and fitting the OH 6-1P1e,1f (4.5) telluric line with a 1D Gaussian. Accordingly, the measured instrument dispersion is convolved with the intrinsic width of the OH 6-1P1e,1f (4.5) telluric line. We assume that the intrinsic width of this telluric line is on the order of the natural line width of Hα emission and is already accounted for in our correction for the instrument line-spread function. The instrument line profile derived from the 1D Gaussian fit to the stacked sky background line is shown in Figure 2. While fitting calibration lamp data would be higher signal-to-noise, a single lamp exposure underestimates the instrument profile as it does not include the jitter introduced in the observation and stacking.

$$\mathrm{SNR_{obs}} = \mathrm{SNR}\left(\sigma_{\mathrm{inst}}^2/\sigma^2 + 1\right) \quad (2)$$

To ensure small velocity dispersions below the instrument resolution are measured reliably, we select a signal to noise cut on our observations (SNR_{obs}) such that intrinsic dispersion measurements (σ) are made with SNR $= \sigma/\delta\sigma = 3$. The observed signal-to-noise (SNR_{obs}) required to reach an intrinsic dispersion measurement with an SNR of 3 is given by Equation 2 (derived in Zhou et al. (2017)). Measuring gas dispersions dominated by thermal broadening and natural line width ($\sigma =\sim 12$ km s^{-1}) with a SNR of 3 requires an observational cut of $\mathrm{SNR}_{obs} = 3(\frac{19.02^2}{12^2} + 1) \approx 10$. A conservative noise estimate is determined by selecting regions in the outskirts of the background subtracted image and creating a histogram of summed counts in a rolling rectangular aperture with dimensions (w,h) = (5,4) pixels. This aperture size corresponds to emission with a velocity width of 64 km s^{-1}, on par with the broadest spectra seen in the disk NGC 7331. The signal is extracted in identical apertures. While the maps presented in Figure 3 and Figure 4 use an observed signal to noise cut of SNR$>$ 3, the dispersion measurements in Figure 5 and Table 2 use an observed signal to noise cut of SNR$>$ 10 in order to achieve a 3σ measurement of dispersions below the instrument resolution (down to 12 km s^{-1}).

Table 1: NGC 7331 CHαS observational summary

Parameter	Value	Comment
Observation Summary		
Right Ascension (α)	22:37:04	FOV Center
Declination (δ)	+34:24:56	FOV Center
Distance	14.5 Mpc	14.7±0.6
Systemic ($\mathrm{V_{Hel}}$)	816 ± 1 km s^{-1}	
Exposure Time	360 s	per frame
Total Integration	2.1 hrs	21 frames
Moon Illumination	$<$ 2%	
Moon Separation	$>$ 125°	
Dates	19 Oct 2023	
Heliocentric Correction	29.54 km s^{-1}	
Instrument Settings		
Field of View	$10' \times 10'$	
Spatial Resolution	$2.8''$	
Spectral Resolution ($\Delta\lambda$)	0.67 Å	
Central Wavelength (λ)	6582 Å	
Bandpass (FWHM)	20 Å	

3.3. *HII Region Selection*

The full catalog of HII regions used in this work is presented in Table 2. The apertures selected are taken from the Petit (1998) [P98] catalog, the Marcelin et al. (1994) catalog, and the Hodge & Kennicutt (1983) [HK83] catalog of HII regions in NGC 7331. We keep the literature IDs for reference, but note that the apertures used may not be positioned exactly as originally intended, and any reproductions of this work should rely on the J2000 coordinates provided in Table 2. A 2D Gaussian was fit to each region, and small adjustments on the order of a few arcseconds were made to the region centroids. The HK83 coordinates were shifted by up to $\sim \pm 4$ arcsec in order to match HII regions in the SINGS Hα image. This offset is due to a combination of factors including the distortion error associated with the 0.9-m plates used to construct this catalog (Hodge & Kennicutt 1983) and differences in blending/resolution between the HK83 and SINGS imaging. We remove re-

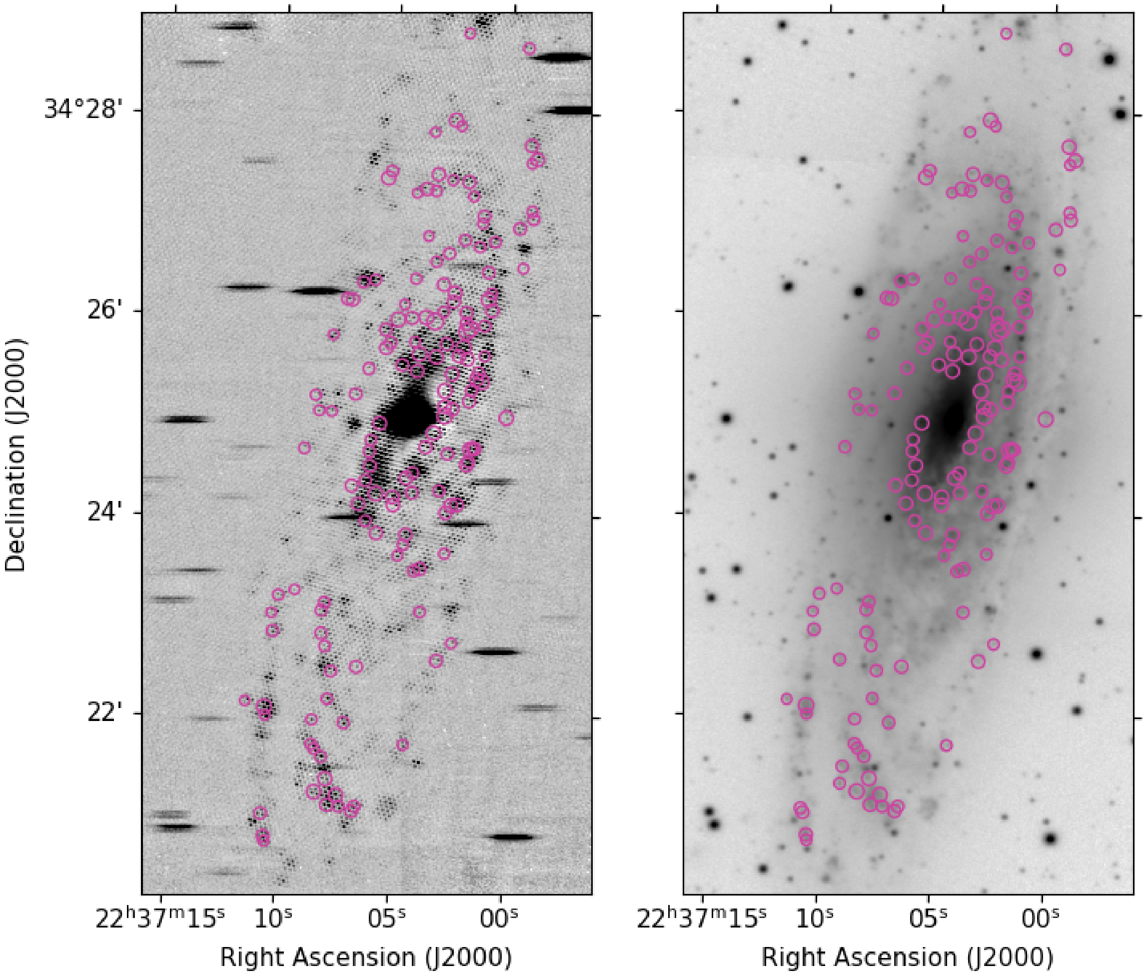

Figure 1: Comparison of CHaS (left) and SINGS (right) images, each overlaid with our catalog of 155 optimized regions represented by 3-sigma radius circles. The regions in the CHaS image have been adjusted based on our high-resolution velocity map to account for spectral shifts and the unique morphology of the lenslets within each region.

gions that are now known stars as well as regions that are contaminated by their proximity to known stars. We also make a cut to only include regions that have a FWHM of $> 4''$, ensuring they are well-matched to our spatial resolution. These regions do not require aperture corrections, as they are resolved by the seeing-limited PSF ($\sim 1'' - 2''$) of the SINGS Hα images (Murphy et al. 2018). The HII regions that remain after this cut are also spatially resolved in the CHαS data, covering at least two lenslets. Finally, we visually inspect all apertures and make a last round of cuts to minimize crowding, reduce the number of blended regions, and remove regions impacted by artifacts such as saturated or over-subtracted pixels.

3.4. *SINGS Aperture Photometry*

We perform aperture photometry to extract flux values from the SINGS data in the apertures shown in Figure 1. We chose an aperture radius corresponding to the effective radius ($\mathrm{r_{eff}} = \sqrt{2\ln 2\sigma_x\sigma_y}$), calculated using the 2D Gaussian fit for each region. The calibration uncertainty is taken to be $\approx 10\%$ of the flux (DR5 Data Delivery Document). The calibration uncertainty dominates over the background error estimated near the edge of the image, so we assume a 10% flux error on the values quoted in Table 2.

4. RESULTS

We report on the ionized gas morphology, luminosity, and kinematics in the disk of NGC 7331. We use these resolved measurements to explore the luminosity-dispersion relation for our sample of HII regions described above.

4.1. *Ionized Gas Morphology*

As shown in Figure 1 the ionized gas morphology seen in the CHαS spectral imaging is consistent with the structure seen in the SINGS narrowband imaging. Stars

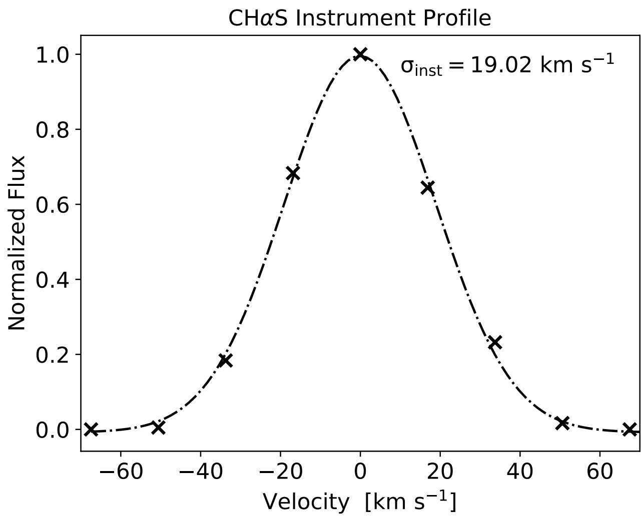

Figure 2: CHαS instrument profile derived from the stacked sky background line in more than 3000 spectra. The instrument dispersion measured from the Gaussian fit shown here is convolved with the (much narrower) intrinsic width of the OH 6-1P1e,1f (4.5) telluric line.

in the CHαS image are dispersed and appear as bright continuum spectra shortened by the narrow bandpass filter. The LINER nucleus (Cowan et al. 1994) is surrounded by faint Hα emission which abruptly increases in brightness due to starburst activity in the inner ring (Battaner et al. 2003). This bright Hα emission is coincident with HI (Bosma 1978) and CO (Young & Scoville 1982) observations of the ring. The outer disk of the galaxy is also bright in discrete Hα emission. The HII regions in our catalog are spread throughout the galactic disk. They range in size from approximately 350 pc − 700 pc. We note that this is not an exhaustive catalog. We leave for future work an algorithmic detection of HII regions (e.g., Sánchez et al. 2012; Espinosa-Ponce et al. 2020; Congiu et al. 2023) which could be applied to a larger sample of galaxies observed during the CHαS commissioning and early science campaigns.

4.2. *Ionized Gas Luminosity*

The Hα luminosity values for HII regions measured in NGC 7331 range from $37.73 < \mathrm{Log}(\mathrm{L}_{\mathrm{H}\alpha}) < 39.16$. The median luminosity of 1×10^{38}erg s^{-1} cm^{-1} corresponds to $\mathrm{Q}_0 = 7.7 \times 10^{49}$ ionizing photons, equivalent to approximately 2 O5 stars, 6 O7 stars, or 21 O9 stars (Table 2.3 in Osterbrock (1974)). Accordingly, the median stellar mass of these regions ranges from 100 $\mathrm{M}_\odot$ − 1000 $\mathrm{M}_\odot$ (assuming an O star mass of 50 $\mathrm{M}_\odot$). The Hα luminosity measurements presented in Table 2 are converted to a star formation rate using the prescription in Calzetti (2013). The total integrated Hα luminosity summed across all of the the selected HII regions corresponds to a SFR of 0.277 $\mathrm{M}_\odot$ yr^{-1}, accounting for about 10% of the total SFR in NGC 7331 (2.987 $\mathrm{M}_\odot$ yr^{-1}) (Leroy et al. 2008). Bright regions are distributed throughout the disk, but almost all HII regions in the inner ring occupy the high end of the luminosity distribution.

4.3. *Resolved Ionized Gas Kinematics*

Maps of the ionized gas velocity and dispersion are made following the spectral fitting procedure described in Section 3.2. The ionized gas velocity map shown in the left panel of Figure 3 recovers the expected clockwise rotation of the galactic disk seen in HI (Walter et al. 2008; Schmidt et al. 2016). This velocity map is well-matched to prior measurements of the ionized gas velocity traced by Doppler shifted Hα emission shown in Marcelin et al. (1994); Daigle et al. (2006). We extend the velocity map to include the high-velocity (redshifted) edge of the galactic disk that is out of the bandpass in previous datasets.

We compare the ionized gas velocity with the neutral gas velocity measured in HI 21 cm emission. The HI velocity field extracted in each lenslet is shown in the left panel of Figure 4. In the right panel of Figure 4 we calculate the residual offset between the ionized gas velocity measured from Hα emission and the neutral gas velocity measured from HI 21cm emission. In order to interpolate over nan values in the large beam size of HI velocity (moment 1) map, we apply small scale median filtering and Gaussian convolution. As a result, the HI velocity map is slightly smoothed. A few spurious values remain in the final HI velocity map that propagate to the residual, but these are easily disregarded when examining the two maps by eye. Small residuals on the order of ± 25 km s^{-1} (one pixel in the CHαS spectra) are within our absolute velocity error bars. Larger residuals, especially those that are spatially coherent over many lenslets, are likely the result of resolution differences (beam smearing) or variation in the neutral and excited gas distributions; however, follow-up analysis is needed to determine if these features may be due to non-rotational, peculiar gas motions. Prominent differences in the velocity map include the redshifted patch in the outer north-west spiral arms and the central asymmetric bi-conical region of high velocity residual aligned with the inner gas ring (CO contours overlaid on Figure 4).

The line-of-sight ionized gas velocity dispersion (σ) is shown in the right panel of Figure 3. This map was created using the spectral fitting procedure described in Section 3.2. We correct the measured dispersion for the instrument profile and thermal broadening. The remaining quantity is the non-thermal line-of-sight ionized

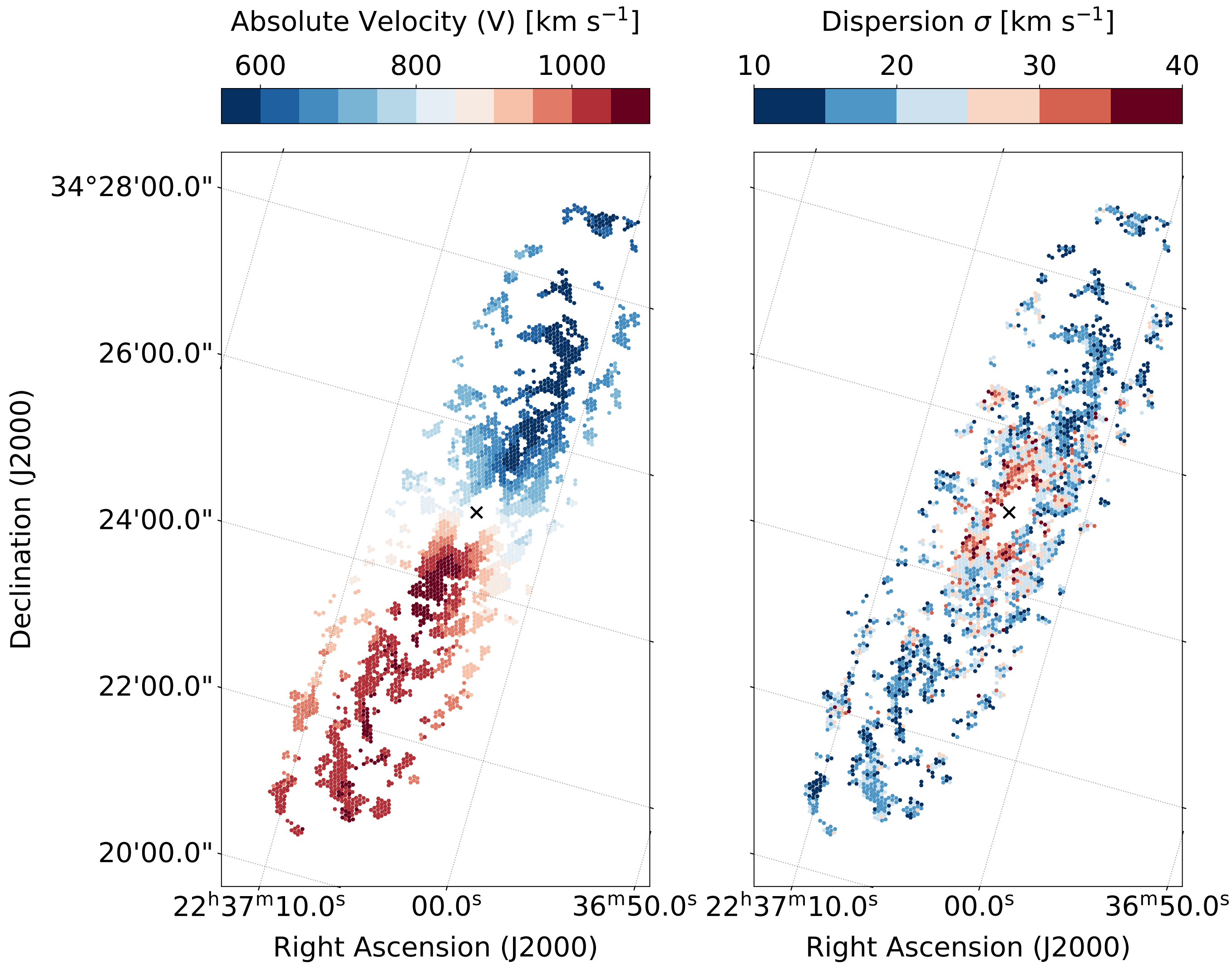

Figure 3: Kinematic measurements derived from the CHαS integral field spectroscopy. In all panels the coordinate system has been rotated (15°) in order to align the hexagonally packed spectra along the Cartesian y-axis. The transformed coordinates can be compared directly with Figure 1. We apply a SNR cut, only displaying detections in lenslets with SNR ≥ 3. The X marker denotes the galactic center coordinates. The individual panel descriptions are as follows: (left) absolute velocity measured in each CHαS lenslet (right) line-of-sight ionized gas velocity dispersion measured in each CHαS lenslet.

gas velocity dispersion referred to as velocity dispersion throughout the rest of the text. Since all spectra were fit as a single emission line component, this analysis does not account for nonsymmetric features in the line profiles or for multiple peaks from additional resolved velocity components. The average velocity dispersion across all measured spaxels (with an SNR cut of 10) is 20.6 ± 4.7 km s^{-1}, and the (slightly lower) median dispersion across all spaxels is 19.7 km s^{-1}. In the outskirts of the galactic disk measured velocity dispersions are at or near at the thermal dispersion limit. Patches of low dispersion that overlap the right inner region of the galaxy may be part of a spiral arm seen in projection, ending in the north of the galaxy. The presence of a complex warp in NGC 7331 has already been inferred on large scales from the HI distribution and velocity field and Bosma (1981) uses the HI velocity field to suggest that the northern arm is warped out of the plane. Evidence of a warp is also seen in the inner disk from a gradient in rotation speed between the stars and emission line gas (Bottema 1999). We discuss sources of confusion and contamination in these kinematic maps in Section 5.2.

4.4. *Luminosity-Dispersion Relation*

In Figure 5 we show the observed L-σ relation for our selected HII regions in NGC 7331, plotting the Hα lumi-

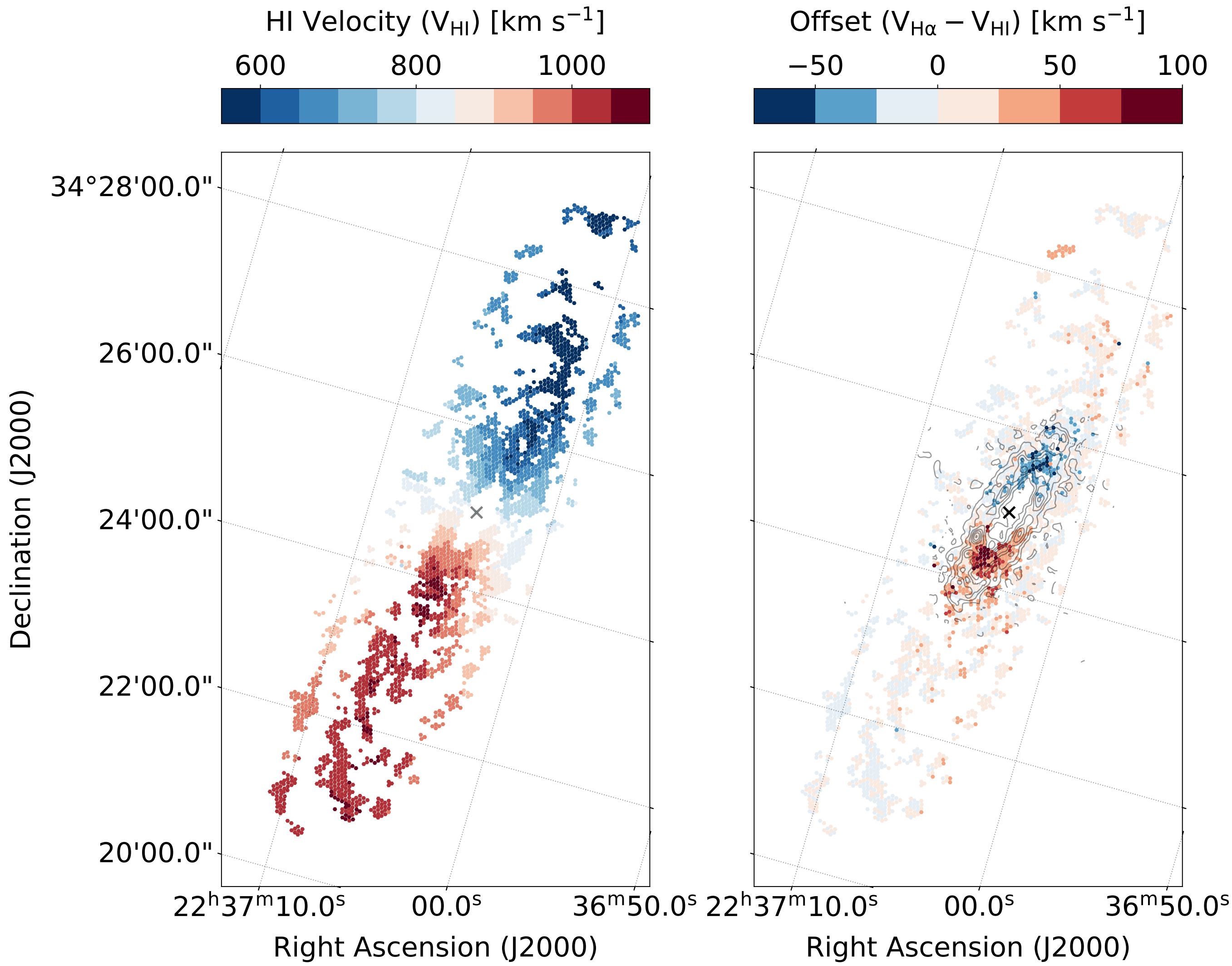

Figure 4: Kinematic measurements derived from the CHαS integral field spectroscopy. In all panels the coordinate system has been rotated (15°) in order to align the hexagonally packed spectra along the Cartesian y-axis. The transformed coordinates can be compared directly with Figure 1. We apply a SNR cut, only displaying detections in lenslets with SNR ≥ 3. The X marker denotes the galactic center coordinates. The individual panel descriptions are as follows: (left) HI 21cm moment 1 velocity field from The HI Nearby Galaxy Survey (THINGS) (Walter et al. 2008). This data has been extracted in regions corresponding to each CHαS lenslet (right) Residual offset between the Hα velocity map and the HI velocity map. The gray contours correspond to the inner gas ring seen in the BIMA SONG CO (1-0) intensity map.

nosity of the HII regions as a function of their average ionized gas velocity dispersion. We only include HII regions with non-thermal motions, meaning those above a threshold of $\sigma > \sqrt{\sigma_{\rm N}^2 + \sigma_{\rm b}^2}$ or $\sigma > 12$ km s^{-1}. We calculate both the average velocity dispersion and the average velocity dispersion weighted by the Hα intensity. However, since the Hα intensity within each region does not vary drastically, this weighting does not change the result significantly and the average velocity dispersion shown in Figure 5 is unweighted.

The HII region properties measured in NGC 7331 are consistent with spatially resolved observations of HII regions in large surveys of nearby galaxy disks. In the top panel of Figure 5 we compare with HII regions in the PHANGS–MUSE nebular catalog (Congiu et al. 2023; Groves et al. 2023). Similar to NGC 7331, a few galaxies in the PHANGS-MUSE survey also have nuclear star forming rings. The blue markers overplotted are HII regions in the nuclear star forming ring of NGC 4321, NGC 3351, and NGC 1672. In order to ensure a direct comparison, we subtract the natural line width and thermal broadening (in quadrature) from the MUSE Hα dispersion measurements and apply a radius cut of 2″ to match the resolution of our data. The L-σ distribution of HII regions in the PHANGS-MUSE catalog is shown as a red 2-D histogram. In the bottom panel we compare with gas dispersions from the SAMI Galaxy Survey shown in light blue (Zhou et al. 2017). We similarly subtract thermal broadening and natural line width in quadrature from these dispersion measurements to make a direct comparison. The SAMI observations already have a reasonably well-matched spatial resolution of 2.5″, so no resolution cut is applied.

We separate HII regions in NGC 7331 into two populations: those in the nuclear star forming ring and those distributed throughout the rest of the galactic disk. The boundary of the inner ring used in this work is determined from the BIMA CO intensity map and is defined as an ellipse centered on (α,δ) = (22h37m3.9s, +34d24m55.4s) with a major axis $2a = 150''$ and a minor axis $2b = 60''$ at an angle of -16 degrees (clockwise). There is a trend of high luminosity HII regions in the inner ring having elevated velocity dispersions when compared with HII regions in the rest of the galactic disk. We discuss processes that may be driving these high velocity dispersions in the inner ring of NGC 7331 in Section 5.

5. DISCUSSION

Our data are consistent with measurements from large surveys of HII regions, including the PHANGS-MUSE Survey (Congiu et al. 2023; Groves et al. 2023) and the SAMI Galaxy Survey (Zhou et al. 2017). Here, we discuss sources of turbulence driving the velocity dispersions measured in our sample of HII regions alongside caveats to these measurements and potential avenues for future work.

5.1. *Turbulence Drivers*

Past studies of giant HII regions have looked for an envelope to the L-σ relation or the lowest non-thermal dispersion at a given luminosity (Terlevich & Melnick 1981; Arsenault et al. 1990; Relaño et al. 2005; Zaragoza-Cardiel et al. 2015). We show a range of models (hatched shading) for this envelope in the top panel of Figure 5. Regions along this envelope are density bounded, their velocity dispersions are primarily driven by virial motions, and their masses can be approximated from the virial theorem (Rozas et al. 1998; Beckman et al. 2000; Relaño et al. 2005; Rozas et al. 2006; Blasco-Herrera et al. 2010). A small subset of the most luminous, early-stage HII regions near virial equilibrium may lie on or near the L-σ envelope. These regions have gravity-driven turbulence. Regions far from this envelope have

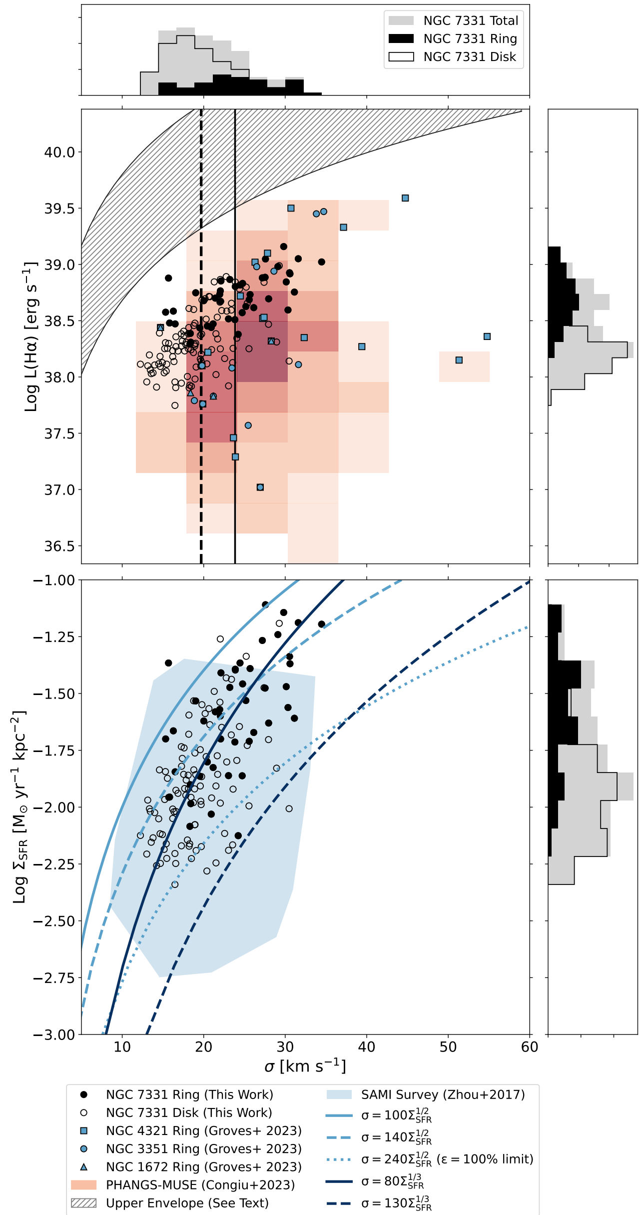

Figure 5: Average ionized gas velocity dispersion in extragalactic HII regions as a function of their Hα luminosity (top) and star formation rate surface density (bottom). The black points represent the HII regions in NGC 7331 from this work, and they are divided into two populations: those in the nuclear star-forming ring (filled) and those distributed throughout the rest of the galactic disk (open). Corresponding histograms for the disk, ring, and total populations are shown along the sides. We compare our catalog with HII regions in the PHANGS-MUSE catalog (red 2D histogram) (Congiu et al. 2023) and the SAMI Galaxy Survey (light blue shading) (Zhou et al. 2017). Models shown are from (Lehnert et al. 2009). See text for more details.

kinematics dominated by contributions from additional processes. We find that, while some of the brightest HII regions in NGC 7331 may fall on/near the L-σ envelope after correcting for intrinsic extinction (see Section 5.2), the majority of HII regions in the disk and ring appear to be driven by alternate processes. This is not surprising, as turbulence driven by gravitational collapse requires massive giant molecular clouds with Jeans Masses on the order of $10^8 M_\odot$ and produces relatively low velocity dispersions with an upper limit on the order of 15 km s^{-1} over our range in $\Sigma_{\rm SFR}$ (Lehnert et al. 2009; Zhou et al. 2017). Accordingly, we explore other sources of energy injection.

If intense star formation is injecting energy into the ISM, turbulence is likely a combination of larger-scale bulk motions (outflows/shocks that accelerate the surrounding material) and smaller-scale random motions (energy transferred to dense regions and eventually dissipated) (Lehnert et al. 2009). In the bottom panel of Figure 5 we compare with energy injection models formulated as a simple scaling relationship $\sigma \propto (\epsilon \dot{E})^\alpha$ (Dib et al. 2006; Lehnert et al. 2009). Here ϵ is the coupling efficiency of the injected energy transferred to the ISM. If turbulence is driven by star formation feedback then the energy injected per unit area should be correlated with the star formation rate surface density $\sigma \propto \epsilon(\Sigma_{\rm SFR})^\alpha$ (Lehnert et al. 2009; Green et al. 2010; Le Tiran et al. 2011; Swinbank et al. 2012a; Lehnert et al. 2013; Green et al. 2014; Moiseev et al. 2015). For dispersions driven by bulk motions such as supernova explosions, this proportion goes as $\sigma \propto \epsilon\Sigma_{\rm SFR}^{1/2}$. Here the coupling factor for energy injected into the ISM ranges from $\epsilon = 100 - 240$ for efficiencies of $25\% - 100\%$ (Dib et al. 2006). If instead energy from star formation is dissipated as turbulence dominated by random motions, a steeper model $\sigma \propto \epsilon\Sigma_{\rm SFR}^{1/3}$ has been proposed to fit the dispersion. Here $\epsilon = 80 - 130$ on 1 kpc injection scales for coupling efficiencies of $25\% - 100\%$ (Lehnert et al. 2009). The steeper model ($\alpha = 1/3$) provides a reasonably good fit to most regions, though some of the HII regions measured require an unphysically large coupling efficiencies of 100% in either model.

Constraining the coupling efficiency to $80 < \epsilon < 240$, we find a best fit relationship to all HII regions in NGC 7331 of $\sigma \propto 80\Sigma_{\rm SFR}^{0.335}$. When we separate the disk and ring populations, the fit for HII regions in the ring reveals a slightly shallower relationship ($\alpha = 0.338$) than the fit for HII regions in the disk ($\alpha = 0.328$). The shallower relationship in the ring could suggest bulk motions contribute to the dispersion; however, due to scatter in these measurements, this measured variation is likely not significant. Many studies have found a similar power law relation with $1/3 < \alpha < 1/2$ (Lehnert et al. 2009; Zhou et al. 2017; Patrício et al. 2018; Yu et al. 2019; Cui et al. 2024). Power law values within this range are notably lower than the $\sigma - \Sigma$ relationship expected from the Kennicutt-Schmidt scaling law, which for a marginally stable disk (Q $\sim$ 1) predicts $\sigma \propto \Sigma_{\rm SFR}^{0.7}$ (Toomre 1964; Kennicutt 1998; Krumholz & Burkert 2010; Krumholz et al. 2012; Swinbank et al. 2012b).

Increased velocity dispersions in the center of galaxies including our own Milky Way is sometimes attributed to shear/ differential rotation in the disk; however, this process increases the dispersion while suppressing star formation, a scenario that is unlikely to explain the increased dispersion seen in the inner ring of NGC 7331 where star formation is enhanced (Krumholz et al. 2017; Federrath et al. 2016; Kruijssen 2017; Federrath et al. 2017). We note that shear may still be contributing in regions with high dispersion and low $\Sigma_{\rm SFR}$. In our catalog, only about 10% of HII regions are both above the median in dispersion and below the median in $\Sigma_{\rm SFR}$. The radial transport of gas through the disk can also drive turbulent gas motions (Krumholz et al. 2018). However, without a wider range in star formation rate, turbulence driven by gas transport is not easily differentiated from turbulence driven by a combination of feedback and transport (Krumholz et al. 2018; Varidel et al. 2020). Further modeling of the disk rotation is needed to compare with the observed velocity map and assess the degree of ionized gas transport in the disk of NGC 7331 (Mai et al. 2024).

5.2. *Caveats*

Beam smearing or the combination of differing line-of-sight velocities due to low spatial resolution can increase the measured velocity dispersion (Epinat et al. 2010; Davies et al. 2011). Beam smearing is most severe at high redshifts (low spatial resolutions) and in galaxies with larger inclinations. Large velocity gradients at the centers of galaxies can also amplify the effects of beam smearing, spuriously increasing the line-of-sight velocity dispersion. To ensure we are not overestimating the velocity dispersion, especially in the inner ring of NGC 7331, we calculate the velocity gradient in each lenslet and confirm that there are not lenslets where $v_g > 2\sigma$ (e.g., Bassett et al. 2014; Varidel et al. 2016; Zhou et al. 2017).

A significant fraction of ionized gas emission occurs beyond HII regions, emanating from the diffuse ionized gas (DIG) between spiral arms. The DIG has been shown to exhibit large velocity dispersions, and measurements of patchy bright complexes may contain an underlying contribution from this broad diffuse emission

(Thurow & Wilcots 2005; Oey et al. 2007). Due to our high signal to noise cut, we do not expect our spectra to be significantly contaminated by broad faint emission from the DIG. We leave for future work an examination of broad and multi-component spectra and lower SNR diffuse regions that may be associated with elevated velocity dispersions.

NGC 7331 is host to many well-known dust features, with dust distributed throughout the spiral arms and prominent dust lanes seen in the western galactic disk. The central star forming ring is also dusty; it appears bright in 24μm images but is absent in GALEX UV data, likely the result of substantial dust extinction (Thilker et al. 2007). The SINGS NGC 7331 Hα map used here is corrected for Galactic foreground extinction but not for intrinsic extinction. For a direct comparison, we do not use the E(B-V) extinction corrections for the PHANGS-MUSE and SAMI survey when plotting these datasets in Figure 5. Bright HII regions in NGC 7331 that are enshrouded in dust will have a significantly lower observed flux/luminosity. Additionally, an inhomogeneous dust distribution that produces varying intrinsic extinction complicates the interpretation of relative flux/luminosity values for HII regions in spatially distinct environments, such as the disk vs the ring. We acknowledge that uncertainties in the intrinsic reddening correction may weaken the derived correlation between $\sigma - \mathrm{SFR}(\mathrm{L}_{\mathrm{H}\alpha})$, with a stronger correlation often noted between $\sigma - \mathrm{SFR}(\mathrm{L}_{\mathrm{IR}})$ (Arribas et al. 2014). Follow-up observations with CHαS in the narrowband Hβ mode (Sitaram et al. 2024) would allow us to estimate our own extinction corrections for NGC 7331 and future targets. Corrections for intrinsic extinction have been previously derived in NGC 7331 by Thilker et al. (2007), finding a global $A_{\mathrm{FUV}} = 2.51$ in the disk and $A_{\mathrm{FUV}} = 3.3$ in the ring. Following Thilker et al. (2007), we assume that the dust structure in NGC 7331 is similar to the Milky Way. Using the Milky way extinction curve from Cardelli et al. (1989), $A_{\mathrm{FUV}} = 2.64A_{\mathrm{V}}$ at $\lambda_{eff} = 1516$ for the GALEX FUV channel (Morrissey et al. 2007) and $A_{\mathrm{H}\alpha} = 0.82A_{\mathrm{V}}$. Accordingly, HII regions in the disk of NGC 7331 have $A(\mathrm{H}\alpha) = 0.78$ and HII regions in the ring have $A(\mathrm{H}\alpha) = 1.02$. Accounting for this intrinsic extinction increases the flux/luminosity values by a factor of 2 (0.3 dex) in the disk and up to 2.5 (0.4 dex) in the ring. Accordingly, correcting for intrinsic extinction in Figure 5 places some of the brightest HII regions on/near the L-σ envelope, implying they are near virial equilibrium (See Section 5.1).

6. SUMMARY

1. We investigate the ionized gas kinematics of HII regions in the disk of NGC 7331 using IFU spectral imaging collected with the Circumgalactic Hα Spectrograph (CHαS). We catalog > 150 HII regions distributed throughout the disk, ranging in diameter from approximately 350 pc $-$ 700 pc. Many of these regions fall within the inner ring of dust and gas, which hosts one-third of the galaxy's current star formation activity.
2. High-resolution velocity and dispersion maps of NGC 7331 are presented in this work, selecting spaxels with high signal-to-noise in order to measure dispersions as low as 12 km s^{-1}. Prominent residuals in the $\mathrm{V}_{\mathrm{H}\alpha} - \mathrm{V}_{\mathrm{HI}}$ map are likely the result of resolution differences (beam smearing) or variation in the neutral and excited gas distributions; however, follow-up analysis of these features is needed to look for peculiar gas motions.
3. The L(Hα), Σ_{SFR} and σ measurements we make in NGC 7331 are consistent with spatially resolved observations of HII regions in large surveys of nearby galaxy disks. The dispersion is correlated with the star formation rate surface density, suggesting that models for intense star formation injecting energy into the ISM are a favorable fit to HII regions in NGC 7331. Using the relation $\sigma \propto \epsilon \Sigma_{\mathrm{SFR}}^{\alpha}$ HII regions in NGC7331 are best fit by $\epsilon = 80$, $\alpha = 0.335$. The best fit varies slightly but not significantly between the ring and the disk, hindered by scatter.
4. En-route to ultra-deep observations of the circumgalactic medium, CHαS will obtain detailed spectral imaging of a large sample of nearby galaxy disks. The methods used in this pilot study will be applied to a larger sample of galaxies observed during the CHαS early science campaigns.

The Circumgalactic Hα Spectrograph is funded by NSF AST-1407652. Nicole Melso is supported by the Alan Brass Prize Fellowship in Instrumentation and Technology Development. Meghna Sitaram is supported by NASA FINESST 80NSSC22K1603. CHαS data was collected at the MDM Observatory, operated by Dartmouth College, Columbia University, Ohio State University, Ohio University, and the University of Michigan. Many thanks to the MDM Observatory staff Eric Galayda and Tony Negrete for their help setting up these observations and installing CHαS on the Hiltner 2.4-meter. Thank you to John Thorstensen and Jules Halpern for their support in scheduling these observations. Thank you to Rob Kennicutt and Sean Linden for helpful discussions that have improved this work.

Facilities: MDM:2.4m, KPNO:2.1m

REFERENCES

Arribas, S., Colina, L., Bellocchi, E., Maiolino, R., & Villar-Martín, M. 2014, A&A, 568, A14, doi: 10.1051/0004-6361/201323324

Arsenault, R., Roy, J. R., & Boulesteix, J. 1990, A&A, 234, 23

Bacchini, C., Fraternali, F., Iorio, G., et al. 2020, A&A, 641, A70, doi: 10.1051/0004-6361/202038223

Bassett, R., Glazebrook, K., Fisher, D. B., et al. 2014, MNRAS, 442, 3206, doi: 10.1093/mnras/stu1029

Battaner, E., Mediavilla, E., Guijarro, A., Arribas, S., & Florido, E. 2003, A&A, 401, 67, doi: 10.1051/0004-6361:20020997

Beckman, J. E., Rozas, M., Zurita, A., Watson, R. A., & Knapen, J. H. 2000, AJ, 119, 2728, doi: 10.1086/301380

Bellocchi, E., Arribas, S., Colina, L., & Miralles-Caballero, D. 2013, A&A, 557, A59, doi: 10.1051/0004-6361/201221019

Blasco-Herrera, J., Fathi, K., Beckman, J., et al. 2010, MNRAS, 407, 2519, doi: 10.1111/j.1365-2966.2010.17078.x

Blauensteiner, M., Remmel, P., Riepe, P., et al. 2017, Astrophysics, 60, 295, doi: 10.1007/s10511-017-9482-9

Bosma, A. 1978, PhD thesis, University of Groningen, Netherlands

—. 1981, AJ, 86, 1825, doi: 10.1086/113063

Bottema, R. 1999, A&A, 348, 77, doi: 10.48550/arXiv.astro-ph/9902240

Calzetti, D. 2013, in Secular Evolution of Galaxies, ed. J. Falcón-Barroso & J. H. Knapen, 419

Cardelli, J. A., Clayton, G. C., & Mathis, J. S. 1989, ApJ, 345, 245, doi: 10.1086/167900

Cevallos-Aleman, I., Schiminovich, D., Sitaram, M., et al. 2024, in Society of Photo-Optical Instrumentation Engineers (SPIE) Conference Series, Vol. 13096, Ground-based and Airborne Instrumentation for Astronomy X, ed. J. J. Bryant, K. Motohara, & J. R. D. Vernet, 1309643, doi: 10.1117/12.3019501

Congiu, E., Blanc, G. A., Belfiore, F., et al. 2023, VizieR Online Data Catalog: Catalogue of classified nebulae (Congiu+, 2023), VizieR On-line Data Catalog: J/A+A/672/A148. Originally published in: 2023A&A...672A.148C, doi: 10.26093/cds/vizier.36720148

Cosens, M., Wright, S. A., Murray, N., et al. 2022, ApJ, 929, 74, doi: 10.3847/1538-4357/ac52f3

Cowan, J. J., Romanishin, W., & Branch, D. 1994, ApJL, 436, L139, doi: 10.1086/187652

Cui, J., Gu, Q., Lu, S., et al. 2024, ApJ, 975, 124, doi: 10.3847/1538-4357/ad77a1

Daigle, O., Carignan, C., Amram, P., et al. 2006, MNRAS, 367, 469, doi: 10.1111/j.1365-2966.2006.10002.x

Davies, R., Förster Schreiber, N. M., Cresci, G., et al. 2011, ApJ, 741, 69, doi: 10.1088/0004-637X/741/2/69

de Vaucouleurs, G., de Vaucouleurs, A., Corwin, Herold G., J., et al. 1991, Third Reference Catalogue of Bright Galaxies

Dib, S., Bell, E., & Burkert, A. 2006, ApJ, 638, 797, doi: 10.1086/498857

Elmegreen, B. G., & Scalo, J. 2004, ARA&A, 42, 211, doi: 10.1146/annurev.astro.41.011802.094859

Epinat, B., Amram, P., Balkowski, C., & Marcelin, M. 2010, MNRAS, 401, 2113, doi: 10.1111/j.1365-2966.2009.15688.x

Espinosa-Ponce, C., Sánchez, S. F., Morisset, C., et al. 2020, MNRAS, 494, 1622, doi: 10.1093/mnras/staa782

Federrath, C., Rathborne, J. M., Longmore, S. N., et al. 2016, ApJ, 832, 143, doi: 10.3847/0004-637X/832/2/143

Federrath, C., Rathborne, J. M., Longmore, S. N., et al. 2017, in IAU Symposium, Vol. 322, The Multi-Messenger Astrophysics of the Galactic Centre, ed. R. M. Crocker, S. N. Longmore, & G. V. Bicknell, 123–128, doi: 10.1017/S1743921316012357

Freedman, W. L., Madore, B. F., Gibson, B. K., et al. 2001, ApJ, 553, 47, doi: 10.1086/320638

Ginzburg, O., Dekel, A., Mandelker, N., & Krumholz, M. R. 2022, MNRAS, 513, 6177, doi: 10.1093/mnras/stac1324

Glazebrook, K. 2013, PASA, 30, e056, doi: 10.1017/pasa.2013.34

Green, A. W., Glazebrook, K., McGregor, P. J., et al. 2010, Nature, 467, 684, doi: 10.1038/nature09452

—. 2014, MNRAS, 437, 1070, doi: 10.1093/mnras/stt1882

Groves, B., Kreckel, K., Santoro, F., et al. 2023, MNRAS, 520, 4902, doi: 10.1093/mnras/stad114

Helfer, T. T., Thornley, M. D., Regan, M. W., et al. 2003, ApJS, 145, 259, doi: 10.1086/346076

Hodge, P. W., & Kennicutt, R. C., J. 1983, AJ, 88, 296, doi: 10.1086/113318

Kennicutt, Robert C., J., Armus, L., Bendo, G., et al. 2003, PASP, 115, 928, doi: 10.1086/376941

Kennicutt, Jr., R. C. 1998, ApJ, 498, 541, doi: 10.1086/305588

Kruijssen, J. M. D. 2017, in IAU Symposium, Vol. 322, The Multi-Messenger Astrophysics of the Galactic Centre, ed. R. M. Crocker, S. N. Longmore, & G. V. Bicknell, 64–74, doi: 10.1017/S1743921316012138

Krumholz, M., & Burkert, A. 2010, ApJ, 724, 895, doi: 10.1088/0004-637X/724/2/895

Krumholz, M. R., & Burkhart, B. 2016, MNRAS, 458, 1671, doi: 10.1093/mnras/stw434

Krumholz, M. R., Burkhart, B., Forbes, J. C., & Crocker, R. M. 2018, MNRAS, 477, 2716, doi: 10.1093/mnras/sty852

Krumholz, M. R., Dekel, A., & McKee, C. F. 2012, ApJ, 745, 69, doi: 10.1088/0004-637X/745/1/69

Krumholz, M. R., Kruijssen, J. M. D., & Crocker, R. M. 2017, MNRAS, 466, 1213, doi: 10.1093/mnras/stw3195

Le Tiran, L., Lehnert, M. D., van Driel, W., Nesvadba, N. P. H., & Di Matteo, P. 2011, A&A, 534, L4, doi: 10.1051/0004-6361/201117609

Lehnert, M. D., Le Tiran, L., Nesvadba, N. P. H., et al. 2013, A&A, 555, A72, doi: 10.1051/0004-6361/201220555

Lehnert, M. D., Nesvadba, N. P. H., Le Tiran, L., et al. 2009, ApJ, 699, 1660, doi: 10.1088/0004-637X/699/2/1660

Leroy, A. K., Walter, F., Brinks, E., et al. 2008, AJ, 136, 2782, doi: 10.1088/0004-6256/136/6/2782

Leroy, A. K., Bigiel, F., de Blok, W. J. G., et al. 2012, AJ, 144, 3, doi: 10.1088/0004-6256/144/1/3

Ludwig, J., Pasquali, A., Grebel, E. K., & Gallagher, III, J. S. 2012, AJ, 144, 190, doi: 10.1088/0004-6256/144/6/190

Mac Low, M.-M., & Klessen, R. S. 2004, Reviews of Modern Physics, 76, 125, doi: 10.1103/RevModPhys.76.125

Mai, Y., Croom, S. M., Wisnioski, E., et al. 2024, MNRAS, 533, 3878, doi: 10.1093/mnras/stae2033

Marcelin, M., Petrosian, A. R., Amram, P., & Boulesteix, J. 1994, A&A, 282, 363

McLeod, A. F., Kruijssen, J. M. D., Weisz, D. R., et al. 2020, ApJ, 891, 25, doi: 10.3847/1538-4357/ab6d63

Melso, N., Schiminovich, D., Smiley, B., et al. 2022, ApJ, 941, 185, doi: 10.3847/1538-4357/ac9d9c

Moiseev, A. V., Tikhonov, A. V., & Klypin, A. 2015, MNRAS, 449, 3568, doi: 10.1093/mnras/stv489

Morrissey, P., Conrow, T., Barlow, T. A., et al. 2007, ApJS, 173, 682, doi: 10.1086/520512

Murphy, E. J., Dong, D., Momjian, E., et al. 2018, ApJS, 234, 24, doi: 10.3847/1538-4365/aa99d7

Oey, M. S., Meurer, G. R., Yelda, S., et al. 2007, ApJ, 661, 801, doi: 10.1086/517867

Osterbrock, D. E. 1974, Astrophysics of gaseous nebulae

Osterbrock, D. E., Fulbright, J. P., Martel, A. R., et al. 1996, PASP, 108, 277, doi: 10.1086/133722

Patrício, V., Richard, J., Carton, D., et al. 2018, MNRAS, 477, 18, doi: 10.1093/mnras/sty555

Perna, M., Arribas, S., Colina, L., et al. 2022, A&A, 662, A94, doi: 10.1051/0004-6361/202142659

Petit, H. 1998, A&AS, 131, 317, doi: 10.1051/aas:1998267

Prada, F., Gutierrez, C. M., Peletier, R. F., & McKeith, C. D. 1996, ApJL, 463, L9, doi: 10.1086/310044

Regan, M. W., Thornley, M. D., Bendo, G. J., et al. 2004, ApJS, 154, 204, doi: 10.1086/423204

Relaño, M., Beckman, J. E., Zurita, A., Rozas, M., & Giammanco, C. 2005, A&A, 431, 235, doi: 10.1051/0004-6361:20040483

Rickards Vaught, R. J., Sandstrom, K. M., Belfiore, F., et al. 2024, ApJ, 966, 130, doi: 10.3847/1538-4357/ad303c

Rizzo, F., Bacchini, C., Kohandel, M., et al. 2024, A&A, 689, A273, doi: 10.1051/0004-6361/202450455

Rozas, M., Richer, M. G., López, J. A., Relaño, M., & Beckman, J. E. 2006, A&A, 455, 539, doi: 10.1051/0004-6361:20054388

Rozas, M., Sabalisck, N., Beckman, J. E., & Knapen, J. H. 1998, A&A, 338, 15

Rozas, M., Zurita, A., Beckman, J. E., & Pérez, D. 2000, A&AS, 142, 259, doi: 10.1051/aas:2000329

Rubin, V. C., Burbidge, E. M., Burbidge, G. R., Crampin, D. J., & Prendergast, K. H. 1965, ApJ, 141, 759, doi: 10.1086/148160

Sánchez, S. F., Rosales-Ortega, F. F., Marino, R. A., et al. 2012, A&A, 546, A2, doi: 10.1051/0004-6361/201219578

Schmidt, T. M., Bigiel, F., Klessen, R. S., & de Blok, W. J. G. 2016, MNRAS, 457, 2642, doi: 10.1093/mnras/stw011

SINGS Team. 2020, Spitzer Infrared Nearby Galaxy Survey, IPAC, doi: 10.26131/IRSA424

Sitaram, M., Schiminovich, D., Cevallos-Aleman, I., et al. 2024, in Society of Photo-Optical Instrumentation Engineers (SPIE) Conference Series, Vol. 13096, Ground-based and Airborne Instrumentation for Astronomy X, ed. J. J. Bryant, K. Motohara, & J. R. D. Vernet, 1309642, doi: 10.1117/12.3019359

Swinbank, A. M., Smail, I., Sobral, D., et al. 2012a, ApJ, 760, 130, doi: 10.1088/0004-637X/760/2/130

—. 2012b, ApJ, 760, 130, doi: 10.1088/0004-637X/760/2/130

Telesco, C. M., Gatley, I., & Stewart, J. M. 1982, ApJL, 263, L13, doi: 10.1086/183914

Terlevich, R., & Melnick, J. 1981, MNRAS, 195, 839, doi: 10.1093/mnras/195.4.839

Thilker, D. A., Boissier, S., Bianchi, L., et al. 2007, ApJS, 173, 572, doi: 10.1086/516646

Thurow, J. C., & Wilcots, E. M. 2005, AJ, 129, 745, doi: 10.1086/426751

Toomre, A. 1964, ApJ, 139, 1217, doi: 10.1086/147861

Tully, R. B. 1988, Nearby galaxies catalog

Übler, H., Genzel, R., Wisnioski, E., et al. 2019, ApJ, 880, 48, doi: 10.3847/1538-4357/ab27cc

Varidel, M., Pracy, M., Croom, S., Owers, M. S., & Sadler, E. 2016, PASA, 33, e006, doi: 10.1017/pasa.2016.3

Varidel, M. R., Croom, S. M., Lewis, G. F., et al. 2020, MNRAS, 495, 2265, doi: 10.1093/mnras/staa1272

Walter, F., Brinks, E., de Blok, W. J. G., et al. 2008, AJ, 136, 2563, doi: 10.1088/0004-6256/136/6/2563

Young, J. S., & Scoville, N. 1982, ApJL, 260, L41, doi: 10.1086/183866

Yu, X., Shi, Y., Chen, Y., et al. 2019, MNRAS, 486, 4463, doi: 10.1093/mnras/stz1146

Zaragoza-Cardiel, J., Beckman, J. E., Font, J., et al. 2015, MNRAS, 451, 1307, doi: 10.1093/mnras/stv1024

Zhou, L., Federrath, C., Yuan, T., et al. 2017, MNRAS, 470, 4573, doi: 10.1093/mnras/stx1504

Table 2: HII regions

ID	Literature ID	RA (J2000)	DEC (J2000)	Radius 3σ [arcseconds]	Hα Flux [ergs/s/cm^2]	Hα Luminosity [ergs/s]	SFR (Hα) [$M_\odot$/yr]	Dispersion [km/s]
1	M034	339.2799974289881	34.353479623056664	9.27	7.48×10^{-15}	1.88×10^{38}	0.001	18.91
2	M044	339.27610333158464	34.401808138854506	8.62	1.64×10^{-14}	4.13×10^{38}	0.0023	26.14
3	M049	339.2750912	34.41049262866931	7.76	2.53×10^{-14}	6.36×10^{38}	0.0035	23.87
4	M050	339.2750997853362	34.40567777266111	7.99	3.80×10^{-14}	9.57×10^{38}	0.0053	29.1
5	M051	339.27497039090173	34.41243175066703	7.33	3.02×10^{-14}	7.61×10^{38}	0.0042	27.19
6	M053	339.27439414899334	34.408125884906546	8.38	3.35×10^{-14}	8.44×10^{38}	0.0046	30.53
7	M055	339.2723648163001	34.39692250214503	8.68	8.10×10^{-15}	2.04×10^{38}	0.0011	18.41
8	M056	339.27262262255937	34.40349697558669	9.56	1.31×10^{-14}	3.29×10^{38}	0.0018	23.04
9	M062	339.27045072451983	34.42485497953342	8.15	4.47×10^{-14}	1.12×10^{39}	0.0062	31.6
10	M067	339.26791402473305	34.42383851470202	8.6	3.28×10^{-14}	8.26×10^{38}	0.0045	30.59
11	M068	339.2684408318342	34.42867697	7.12	2.15×10^{-14}	5.40×10^{38}	0.003	25.69
12	M070	339.26770787482144	34.42667806525346	9.39	3.06×10^{-14}	7.69×10^{38}	0.0042	27.53
13	M074	339.26634625471115	34.406919607196905	7.95	4.18×10^{-14}	1.05×10^{39}	0.0058	34.47
14	M077	339.2649733660056	34.42620580531687	9.4	2.26×10^{-14}	5.68×10^{38}	0.0031	31.13
15	M080	339.2635184291207	34.42832928706503	8.37	2.84×10^{-14}	7.13×10^{38}	0.0039	22.12
16	M081	339.2634886807107	34.413545209835824	9.41	2.32×10^{-14}	5.82×10^{38}	0.0032	22.04
17	M091	339.2608074773679	34.41750533293591	8.9	1.18×10^{-14}	2.96×10^{38}	0.0016	16.5
18	M101	339.2575474888493	34.42056357	7.42	4.45×10^{-14}	1.12×10^{39}	0.0062	27.58
19	M111	339.2555290173183	34.42624635180776	7.16	2.92×10^{-14}	7.35×10^{38}	0.004	22.04
20	M112	339.2547082	34.43668480772701	7.23	2.50×10^{-14}	6.29×10^{38}	0.0035	25.21
21	M118	339.2505943957495	34.41601801049542	9.43	4.19×10^{-15}	1.05×10^{38}	0.0006	< 12
22	PJ223704.8+342425	339.2672194468452	34.40607252254491	8.89	2.78×10^{-14}	6.99×10^{38}	0.0038	30.13
23	P004	339.24589161376696	34.45891939648461	8.74	6.06×10^{-15}	1.52×10^{38}	0.0008	14.65
24	P006	339.2465487330379	34.448996996973655	7.91	4.48×10^{-15}	1.13×10^{38}	0.0006	15.4
25	P007	339.24675517619005	34.45025575300375	7.34	4.01×10^{-15}	1.01×10^{38}	0.0006	18
26	P008	339.2468522466531	34.45820777860385	6.8	4.59×10^{-15}	1.16×10^{38}	0.0006	13.45
27	P009	339.24711446366314	34.46119923866654	8.67	5.33×10^{-15}	1.34×10^{38}	0.0007	23.55
28	P014	339.2479583275394	34.477384819301435	7.46	3.59×10^{-15}	9.04×10^{37}	0.0005	13.01
29	P015	339.2484267173241	34.44082867670712	6.99	2.58×10^{-15}	6.50×10^{37}	0.0004	< 12
30	P016	339.2492985582072	34.44743269902955	8.23	5.33×10^{-15}	1.34×10^{38}	0.0007	14.93
31	P028	339.25425548551	34.44521260840597	7.26	8.13×10^{-15}	2.05×10^{38}	0.0011	28.94
32	P030	339.2546152	34.43383982841462	8.79	1.35×10^{-14}	3.40×10^{38}	0.0019	21.66
33	P032	339.25575057770385	34.422005045917686	10.12	2.41×10^{-14}	6.05×10^{38}	0.0033	24.39
35	P034	339.25538714251394	34.435644300549164	9.61	1.79×10^{-14}	4.51×10^{38}	0.0025	25.34
36	P035	339.2557330420641	34.43127285993701	7.82	1.62×10^{-14}	4.06×10^{38}	0.0022	18.19
37	P037	339.2556048312991	34.440168882090575	8.03	9.77×10^{-15}	2.46×10^{38}	0.0014	14.57
39	P038	339.25639001564656	34.41085520612168	8.1	1.92×10^{-14}	4.84×10^{38}	0.0027	19.78
40	P040	339.2564038296579	34.423493909743264	8.2	3.01×10^{-14}	7.56×10^{38}	0.0042	15.68
41	P041	339.2566214208914	34.44951560803631	8.29	7.90×10^{-15}	1.99×10^{38}	0.0011	15.7
42	P042	339.2567721248971	34.41101917482906	8.56	2.07×10^{-14}	5.20×10^{38}	0.0029	20.64
43	P043	339.2566648178783	34.422437447326224	9.15	2.92×10^{-14}	7.35×10^{38}	0.004	23.2
44	P047	339.2569614917571	34.448313282864824	7.08	9.61×10^{-15}	2.42×10^{38}	0.0013	17.25
45	P048	339.25745721378286	34.408826208056745	8.16	2.77×10^{-14}	6.98×10^{38}	0.0038	23.88
46	P049	339.2573447386873	34.44439318894881	7.2	1.58×10^{-14}	3.98×10^{38}	0.0022	18.77
47	P052	339.2577084285793	34.41876595776951	8.55	2.23×10^{-14}	5.60×10^{38}	0.0031	19.02
48	P053	339.2573024924532	34.410835219130135	9.26	2.05×10^{-14}	5.16×10^{38}	0.0028	20.75
49	P054	339.2576891984581	34.408250024967955	9.11	2.78×10^{-14}	7.00×10^{38}	0.0038	21.29
50	P058	339.2584660503508	34.452820740740165	6.99	9.24×10^{-15}	2.32×10^{38}	0.0013	17.59
51	P059	339.2589184482859	34.425779188345224	8.72	1.18×10^{-14}	2.97×10^{38}	0.0016	21.16
52	P060	339.2591818231548	34.40160027	8.9	2.76×10^{-14}	6.94×10^{38}	0.0038	27.4
53	P061	339.2595286813322	34.37859706802978	7.03	3.31×10^{-15}	8.34×10^{37}	0.0005	23.05
54	P062	339.2588728727057	34.43086880751817	10.21	1.20×10^{-14}	3.02×10^{38}	0.0017	15.81
55	P063	339.25932323482624	34.45521765162969	8.57	9.04×10^{-15}	2.28×10^{38}	0.0013	16.59
56	P064	339.25901070247824	34.47989189814565	6.7	3.46×10^{-15}	8.71×10^{37}	0.0005	< 12
57	P065	339.2596786331047	34.43167423483792	8.5	1.50×10^{-14}	3.76×10^{38}	0.0021	15.33
58	P066	339.25961487163454	34.430374598519535	10.64	1.09×10^{-14}	2.75×10^{38}	0.0015	20.93
59	P068	339.2598097005033	34.433476070956615	8.24	1.53×10^{-14}	3.84×10^{38}	0.0021	16.28
60	P070	339.2601152087485	34.42774873574997	9.77	1.93×10^{-14}	4.86×10^{38}	0.0027	25.58
61	P071	339.2601648504359	34.40148210826472	8.97	3.10×10^{-14}	7.80×10^{38}	0.0043	22.76
62	P073	339.26010852373577	34.44557597698603	7.87	7.75×10^{-15}	1.95×10^{38}	0.0011	18.88
63	P074	339.26110527993006	34.39350094894859	7.17	7.14×10^{-15}	1.80×10^{38}	0.001	15.55
64	P075	339.26092081673886	34.41006288768159	8.0	1.29×10^{-14}	3.23×10^{38}	0.0018	23.82
65	P077	339.2610300820177	34.40029331238323	8.58	1.97×10^{-14}	4.96×10^{38}	0.0027	20.18

Table 2: HII regions continued

ID	Literature ID	RA (J2000)	DEC (J2000)	Radius 3σ [arcseconds]	Hα Flux [ergs/s/cm^2]	Hα Luminosity [ergs/s]	SFR (Hα) [M$_\odot$/yr]	Dispersion [km/s]
66	P078	339.2607130770804	34.46450183544925	6.85	3.36×10^{-15}	8.44×10^{37}	0.0005	18.28
67	P079	339.2610309101004	34.42630987255479	8.63	2.70×10^{-14}	6.78×10^{38}	0.0037	24.77
68	P080	339.2621051036047	34.41792894597592	8.73	1.89×10^{-14}	4.77×10^{38}	0.0026	20.01
69	P081	339.26168456150634	34.46549368	9.16	4.93×10^{-15}	1.24×10^{38}	0.0007	14.68
70	P084	339.2618591028508	34.43682671574398	8.76	9.61×10^{-15}	2.42×10^{38}	0.0013	18.12
71	P085	339.26192171679327	34.41634831	10.19	1.48×10^{-14}	3.73×10^{38}	0.0021	24.72
72	P086	339.2622950444613	34.37572637277211	8.41	4.18×10^{-15}	1.05×10^{38}	0.0006	21.51
73	P087	339.26179425790696	34.42333355728113	8.99	1.97×10^{-14}	4.95×10^{38}	0.0027	27.97
74	P088	339.2621255844163	34.40392068562348	7.64	2.61×10^{-14}	6.56×10^{38}	0.0036	24.45
75	P089	339.26216638578114	34.43534191772748	8.62	9.68×10^{-15}	2.44×10^{38}	0.0013	18.36
76	P090	339.2621603110673	34.45552709	7.09	1.09×10^{-14}	2.75×10^{38}	0.0015	18.16
77	P091	339.26262681756185	34.420564222111514	9.49	1.87×10^{-14}	4.70×10^{38}	0.0026	22.08
78	P101	339.2628763797871	34.44337436216011	7.79	5.98×10^{-15}	1.50×10^{38}	0.0008	< 12
79	P103	339.26382609634027	34.43362778659859	7.41	1.68×10^{-14}	4.23×10^{38}	0.0023	25.17
80	P104	339.26366386827965	34.43820037	8.63	7.40×10^{-15}	1.86×10^{38}	0.001	16.6
81	P105	339.26449594127325	34.411178600238095	8.55	1.99×10^{-14}	5.02×10^{38}	0.0028	21.42
82	P109	339.2652638703704	34.38384573286964	7.5	3.23×10^{-15}	8.13×10^{37}	0.0004	14.22
83	P110	339.2650768497967	34.44199986996687	7.4	7.92×10^{-15}	1.99×10^{38}	0.0011	19.02
84	P111	339.2653519521519	34.39100371717822	8.51	1.56×10^{-14}	3.93×10^{38}	0.0022	23.38
85	P113	339.2651615462616	34.453731625919545	7.41	5.45×10^{-15}	1.37×10^{38}	0.0008	16.35
86	P114	339.26472826654464	34.45651170734874	8.64	3.12×10^{-15}	7.85×10^{37}	0.0004	< 12
87	P117	339.2654333272613	34.46350915875691	6.74	3.18×10^{-15}	8.00×10^{37}	0.0004	18.21
88	P118	339.2651971727298	34.43207413972957	11.06	9.51×10^{-15}	2.39×10^{38}	0.0013	24.23
89	P119	339.26616363936654	34.403643011902325	8.28	1.13×10^{-14}	2.83×10^{38}	0.0016	20.45
90	P120	339.26641436177886	34.39066392	7.82	1.84×10^{-14}	4.62×10^{38}	0.0025	21.99
91	P122	339.26639150045554	34.44624293660967	6.63	3.60×10^{-15}	9.06×10^{37}	0.0005	< 12
92	P123	339.2666995	34.454088089113974	8.53	4.87×10^{-15}	1.23×10^{38}	0.0007	19.07
93	P124	339.2665757907516	34.43275381515483	9.55	7.80×10^{-15}	1.96×10^{38}	0.0011	18.31
94	P125	339.2678997232997	34.36177769090223	7.06	3.50×10^{-15}	8.81×10^{37}	0.0005	17.27
95	P127	339.26743793761267	34.39668314780908	8.65	1.30×10^{-14}	3.26×10^{38}	0.0018	20.3
96	P129	339.26793410530746	34.39498857968776	7.26	8.80×10^{-15}	2.21×10^{38}	0.0012	24.06
97	P131	339.2685248710373	34.43918753243254	7.34	5.51×10^{-15}	1.39×10^{38}	0.0008	30.48
98	P133	339.2689232772113	34.393213184040185	7.08	9.30×10^{-15}	2.34×10^{38}	0.0013	19.58
99	P135	339.2689039641369	34.43266288227842	8.58	6.81×10^{-15}	1.71×10^{38}	0.0009	16.2
100	P136	339.26855172052365	34.45341146366023	6.69	5.75×10^{-15}	1.45×10^{38}	0.0008	19.58
101	P138	339.26952938882954	34.401602668403015	8.74	1.08×10^{-14}	2.73×10^{38}	0.0015	19.52
102	P141	339.2695183593109	34.402960132031104	8.78	2.15×10^{-14}	5.42×10^{38}	0.003	21.96
103	P142	339.27045829894746	34.43489285177114	7.04	7.11×10^{-15}	1.79×10^{38}	0.001	18.1
104	P145	339.2714198328167	34.43242762988688	9.78	5.20×10^{-15}	1.31×10^{38}	0.0007	20.39
105	P146	339.27256480193705	34.42855831425452	8.16	1.20×10^{-14}	3.01×10^{38}	0.0017	18.92
106	P147	339.27271100025223	34.45705421	7.77	3.11×10^{-15}	7.81×10^{37}	0.0004	< 12
107	P149	339.2733176990918	34.42769979539784	8.65	9.63×10^{-15}	2.42×10^{38}	0.0013	21.5
108	P150	339.2734165817021	34.45591476130711	9.26	2.71×10^{-15}	6.81×10^{37}	0.0004	< 12
109	P153	339.27361616827534	34.43075313720044	8.15	1.55×10^{-14}	3.89×10^{38}	0.0021	22.21
110	P156	339.2744451093311	34.39897149678777	7.41	1.57×10^{-14}	3.94×10^{38}	0.0022	30.34
111	P165	339.27553866430907	34.438998912081864	7.53	1.17×10^{-14}	2.94×10^{38}	0.0016	27.95
112	P169	339.2764346842209	34.37474885791667	8.34	2.16×10^{-15}	5.43×10^{37}	0.0003	< 12
113	P170	339.27668302744667	34.35158063063088	7.81	6.95×10^{-15}	1.75×10^{38}	0.001	20.97
114	P172	339.27629994173566	34.424268678793815	7.82	6.89×10^{-15}	1.73×10^{38}	0.001	< 12
115	P174	339.27728099138614	34.35078560970485	8.12	7.73×10^{-15}	1.95×10^{38}	0.0011	17.81
116	P180	339.2776925145965	34.43864966270467	7.61	3.87×10^{-14}	9.74×10^{38}	0.0054	29.27
117	P184	339.27805578391946	34.40484153	8.37	1.01×10^{-14}	2.55×10^{38}	0.0014	17.54
118	P185	339.2786144895433	34.36546036	7.95	7.10×10^{-15}	1.79×10^{38}	0.001	15.21
119	P186	339.2785214070342	34.42006143739739	8.08	7.07×10^{-15}	1.78×10^{38}	0.001	22.04
120	P188	339.27938487573755	34.43575073696493	8.54	5.80×10^{-15}	1.46×10^{38}	0.0008	22.57
121	P189	339.27954017701944	34.35158272801949	7.69	8.08×10^{-15}	2.03×10^{38}	0.0011	17.85
122	P192	339.2802293239135	34.43588524119142	8.21	7.08×10^{-15}	1.78×10^{38}	0.001	25.56

Table 2: HII regions continued

ID	Literature ID	RA (J2000)	DEC (J2000)	Radius 3σ [arcseconds]	Hα Flux [ergs/s/cm^2]	Hα Luminosity [ergs/s]	SFR (Hα) [M$_\odot$/yr]	Dispersion [km/s]
123	P193	339.2810577066754	34.37406095060599	7.51	5.21×10^{-15}	1.31×10^{38}	0.0007	14.48
124	P198	339.2817119188547	34.36945602800752	7.35	6.78×10^{-15}	1.70×10^{38}	0.0009	17.66
125	P199	339.2821136251674	34.37819753060024	7.43	3.59×10^{-15}	9.03×10^{37}	0.0005	16.47
126	P200	339.2817805858021	34.35182846901407	8.66	1.14×10^{-14}	2.86×10^{38}	0.0016	18.78
127	P201	339.28209650728326	34.35617394781139	9.14	5.17×10^{-15}	1.30×10^{38}	0.0007	15.47
128	P203	339.28264692529507	34.38547008747002	7.57	7.14×10^{-15}	1.80×10^{38}	0.001	23.6
129	P205	339.2830714767444	34.35984689790715	7.73	8.65×10^{-15}	2.18×10^{38}	0.0012	21.71
130	P206	339.28298685384726	34.38035707511662	8.0	4.33×10^{-15}	1.09×10^{38}	0.0006	15.15
131	P207	339.2826450873894	34.41720056	6.91	7.50×10^{-15}	1.89×10^{38}	0.001	17.28
132	P208	339.2830990678638	34.384154389958084	7.78	6.94×10^{-15}	1.75×10^{38}	0.001	18.44
133	P211	339.28263578974617	34.429944892350605	6.71	4.97×10^{-15}	1.25×10^{38}	0.0007	19.64
134	P214	339.2843193501582	34.36120001501291	7.34	8.02×10^{-15}	2.02×10^{38}	0.0011	15.31
135	P215	339.2843043304915	34.35401644470021	9.56	6.36×10^{-15}	1.60×10^{38}	0.0009	19.7
136	P218	339.28486290596703	34.36191512786642	7.53	6.77×10^{-15}	1.70×10^{38}	0.0009	16.85
137	P219	339.28490493713184	34.36601614448407	7.38	3.20×10^{-15}	8.05×10^{37}	0.0004	16.57
138	P220	339.2850907264184	34.41735566814741	7.09	8.19×10^{-15}	2.06×10^{38}	0.0011	< 12
139	P222	339.28582676148966	34.41994075914723	7.19	5.52×10^{-15}	1.39×10^{38}	0.0008	19.68
140	P223	339.28704038522625	34.35815017077321	7.81	6.24×10^{-15}	1.57×10^{38}	0.0009	13.34
141	P224	339.2874592755719	34.35530952374468	7.19	5.08×10^{-15}	1.28×10^{38}	0.0007	13.99
142	P226	339.28751621465483	34.41110143470348	7.5	4.19×10^{-15}	1.06×10^{38}	0.0006	< 12
143	P229	339.2878414	34.375878041583405	7.54	4.32×10^{-15}	1.09×10^{38}	0.0006	13.79
144	P230	339.2885941279833	34.38761296688157	6.79	2.72×10^{-15}	6.85×10^{37}	0.0004	< 12
145	P236	339.2917935800056	34.38675073880019	7.3	3.29×10^{-15}	8.27×10^{37}	0.0005	18.49
146	P238	339.29268702843854	34.38079552941009	7.76	6.55×10^{-15}	1.65×10^{38}	0.0009	18.74
147	P239	339.2929539229114	34.38379279522877	6.62	3.81×10^{-15}	9.59×10^{37}	0.0005	18.94
148	P240	339.29342493061944	34.34589808557353	6.98	8.29×10^{-15}	2.09×10^{38}	0.0011	17.37
149	P241	339.2935327467627	34.346740684014385	8.22	9.56×10^{-15}	2.41×10^{38}	0.0013	19.75
150	P242	339.2937898236852	34.366807339894095	6.88	1.80×10^{-14}	4.52×10^{38}	0.0025	23.41
151	P244	339.2938981003848	34.36821494548739	9.65	1.53×10^{-14}	3.85×10^{38}	0.0021	22.83
152	P245	339.29420012550304	34.350476629767655	8.14	5.16×10^{-15}	1.30×10^{38}	0.0007	12.24
153	P250	339.29459822041235	34.35115542523452	7.65	4.26×10^{-15}	1.07×10^{38}	0.0006	13.56
154	P251	339.29747107559655	34.36920287065264	6.69	5.00×10^{-15}	1.26×10^{38}	0.0007	13.13
155	EO18S001	339.2734292889596	34.41517416883838	8.76	5.73×10^{-14}	1.44×10^{39}	0.0079	29.81